Radiographic image analysis of cylindrical implosion experiments (invited)

J. M. Scott,[a] J. B. Beck, S. H. Batha, C. W. Barnes, and D. L. Tubbs

Los Alamos National Laboratory, P.O. Box 1663, Los Alamos, New Mexico 87545

(Presented on 20 June 2000)

Radiography is a heavily used tool for diagnosing laser-based hydrodynamic experiments. A successful experiment relies on the gathering of data over a time window where the relevant physics occurs and on an accurate analysis of those data. Comparison of this experimental data to theory is often best done by generating simulated images from hydrodynamic calculations, including all necessary and important experimental details. Care must be taken to treat both the experimental and theoretical images identically in the analysis. Frequently, image filtering and enhancement routines are used to obtain interface location and perturbation information from the radiographic image. Previous techniques were found to be too sensitive to global image details. New procedures have been developed which utilize local operators that provide better edge or interface identification without bias. These procedures are benchmarked and validated using static radiographic targets of known configuration that mock up experimental situations of interest. The experiment and the image analysis development are described, including discussion of key contributions to the uncertainty of the results. © *2001 American Institute of Physics.* [DOI: 10.1063/1.1315643]

I. INTRODUCTION

Perturbation growth on the surface of inertial confinement fusion (ICF) capsules seeded by target surface or laser nonuniformities may disrupt an ICF implosion and quench ignition. Typically, ICF capsules suffer from perturbation growth due to the Richtmyer–Meshkov (shock-driven) and Rayleigh–Taylor (acceleration/deceleration-driven) instabilities.[1–4] In a convergent geometry, perturbation growth is enhanced by the Bell–Plesset[5,6] effect even when there is an absence of acceleration at the unstable interface. Interface convergence lowers the threshold for nonlinear saturation of the perturbation by decreasing the wavelength of the perturbation as the implosion proceeds. During the implosion, the mode number stays constant but the radius decreases. Consequently, the wavelength ($\lambda = 2\pi R/m$) of the perturbation decreases, and a given mode will saturate at a lower amplitude as compared to the planar case. The study of convergent hydrodynamics in a cylindrical geometry is of interest because of the direct line-of-sight diagnostic access for the imploding cylinder. An additional advantage is that cylindrical symmetry is consistent with that of numerical grids used in two-dimensional physics codes.

Cylindrical implosion experiments have been conducted in an indirect drive[7,8] (ID) and direct drive[9,10] (DD) configuration at the NOVA and OMEGA laser facilities, respectively. Both campaigns utilize radiographic images to measure ablative Rayleigh–Taylor perturbation growth. Imploding cylinders are imaged along their z axis to give an $r-\theta$ view of the converging cylindrical surface. In these experiments, the perturbed surface is not imaged directly. Perturbation growth at the ablation surface is inferred by the feedthrough of the perturbations to an embedded higher-opacity marker layer. The marker layer is a thin shell of material that is opaque to the x rays from the backlighter. Figure 1 gives a depiction of an imploding cylinder with a perturbed central marker section. An image of the opaque shell is the main result of these experiments. The perturbation is measured by assessing the location of the interface between the opaque shell and the more transparent pusher material.

The experimental data is used for the validation of physics simulation codes, such as LASNEX[11] and RAGE.[12] Comparisons with experiment are made by generating radiographs from the simulation data. The simulated images include all necessary experimental effects. This provides an equivalent comparison between simulation results and experimental data. The same image analysis routines are then applied to the experimental and simulated images to extract information about the perturbation growth. Problems encountered with the image analysis process demonstrated that the process itself could affect the results for both experimental and simulated images. An accurate assessment of the image analysis routines was needed, based on data that could be accurately benchmarked.

II. EXPERIMENT

To benchmark the radiographic image analysis process, an experiment was designed to image an object with a mea-
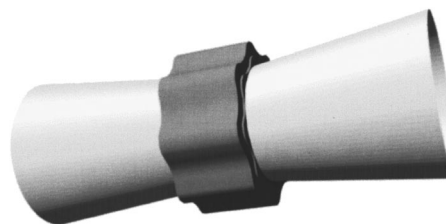

FIG. 1. Illustration of an imploding cylinder with a perturbed central marker section.
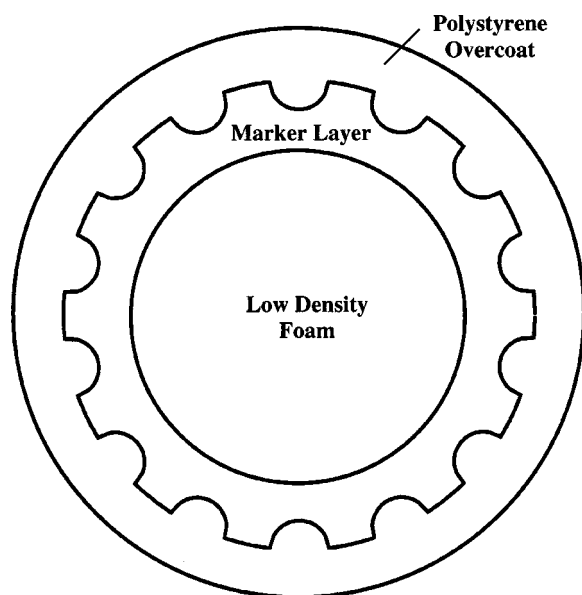
[a] Electronic mail: jmscott@lanl.gov

FIG. 2. Theoretical gear shape of the static target.

FIG. 3. Schematic of a side-on view of a small static target. All dimensions are in microns.

sured, preimposed perturbation. This experiment was developed to be a static experiment with no drive beams interacting with the target. The target would simply be backlit the same way as the dynamic targets in the previous DD cylindrical implosion experiments.[9] Since the image analysis routines to be benchmarked will be used to process dynamic target data, importance was given to designing a static target that had a perturbation amplitude and optical depth similar to that of the dynamic target at different stages during its implosion.

Dynamic targets have been fabricated with several different mode numbers with amplitudes up to a few microns. When imploded, the target is designed so that the amplitude grows to tens of microns. Therefore, the ideal static target would have a sinusoidal perturbation amplitude on the order of 10–30 μm and the appropriate average radius that corresponds to that amount of growth in the dynamic target. Unfortunately, the manufacturing process used to produce a sinusoidal perturbation on dynamic targets is limited to amplitudes of a few microns. The solution was to machine semicircular troughs down the side of a marker layer by dragging the cutting tool with sufficient depth to give appropriate perturbation amplitudes. The resulting shape, shown in Fig. 2, looks like a gear due to the semicircular cutouts. The semicircular troughs are machined in a 62.5 μm thick cylinder to be 25 μm deep using a 25 μm radius-of-curvature tool and are placed to give mode 14 as the fundamental mode. Fourteen troughs around the gear provides sufficient spacing for ease of fabrication. The innermost layer of material is the same low-density foam used in the center of the dynamic targets. The next layer is the marker layer with the semicircular troughs machined into it. The marker layer is overcoated with polystyrene to represent unablated pusher material. The thickness of this outer coat varies but is measured so that it can be included in simulations.

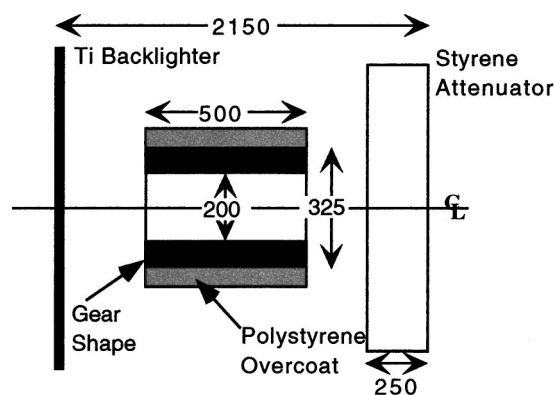A schematic of the small static target is given in Fig. 3. The backlighter material, Ti, is the same for the static and dynamic targets. The gear shape of the static target matches the length of the dichlorostyrene ($C_8H_6Cl_2$) layer seen in the DD experiments, 500 μm, and is called the marker layer. In the dynamic target, the marker layer occupies the central portion of a 2000 μm long cylinder. The other 1500 μm of the cylinder consists of the dynamic ablator. Therefore, to match the optical depth of the static target to the dynamic target it was necessary to add the styrene attenuator shown in Fig. 3. Two different-sized static targets were manufactured; however, they both had the same trough depth. The smaller target has a 200 μm inner diameter for the low-density foam and the larger target has an inner diameter of 400 μm. Two sizes were necessary to test image processing routines with the object corresponding to the dynamic target both when the perturbations have reached maximum growth and midway through the implosion.

Good target characterization was fundamental to the success of this experiment. Important parameters were the perturbation shape and depth. Although theoretical amplitudes from the gear shape can be calculated, in practice this was not the modal spectrum observed when the gear shape was measured by profilometry. Figure 4 gives a measured perturbation profile of a large static target with an overlay of the theoretical shape that would be achieved by machining semicircular troughs. The gear shape was measured with a thin probe that was deflected as the target rotated underneath the probe. From the measurements, there was good peak-to-peak and trough-to-trough consistency. Zooming in on the troughs shows a well rounded shape. Overall, the manufacturing process yielded targets of consistent gear shape that were well characterized by profilometry.

Six static targets were radiographed in a recent experimental campaign. Results from the three large and three small targets will be analyzed and discussed in detail. Experimental images are shown in Figs. 5(a) and 5(b). In each, the bright central circle is the low-density foam. The opaque, gear-shaped marker layer is between the low-density foam and the polystyrene overcoat. The brighter area outside the polystyrene overcoat represents transmission through the styrene attenuator. A leaded-acrylic aperture mounted on the end of the target frames the image with a circle that is too large to fit completely in the image.
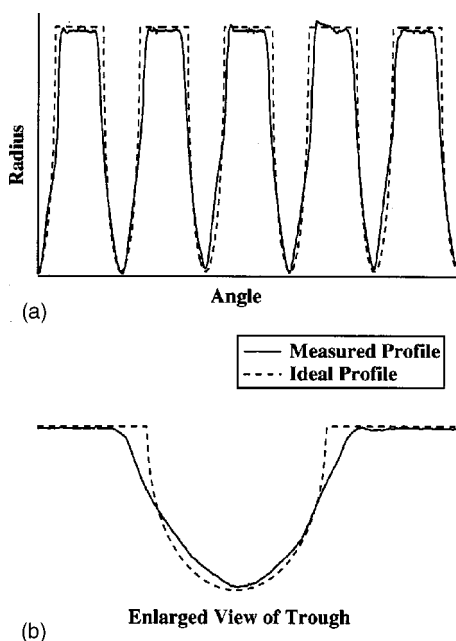
(a)

Measured Profile
Ideal Profile

(b)

FIG. 4. (a) Comparison of lineouts from the measurement of a static target and an ideal profile. (b) An enlarged view of a single trough comparing the ideal profile to a measured profile.

III. FOURIER ANALYSIS ALGORITHM

Ever since the initial cylindrical implosion experiments, the location of the interface in both the experimental and simulated radiographs has been identified by a set of digital filters that operate on the Fourier transform of the image. High frequency components of the image are removed to smooth noise and low frequency components of the image are removed to enhance the edges. Correct operation of these Fourier filters relies on the user choosing the appropriate frequencies to filter the image. While experimental images appeared fairly insensitive to the exact choice of these filters, application to simulated images using these image reduction techniques demonstrated that varying results could be obtained by modest changes in the filter parameters.[10] The high sensitivity of the simulated images to the filtering routines introduced significant uncertainties to the predicted amplitudes.

The static target campaign was originally meant to serve as a benchmark for the Fourier filtering routines. The experimental images in combination with simulated images of the static target would determine the proper filter parameters to choose in the future analysis of cylindrical implosion data. Universal parameters could not be found. Experimental images from different static target shots reacted differently to the same level of filtering. This is due to the fact that the frequency spectrum of the image is highly dependent on the particular geometric shapes in the image and the intensity scale of the image. The Fourier filtration process depends globally on the entire image. Details in one region of the image can affect the entire image analysis. The simulated images do not contain the noise or geometric factors, like microstrip cutoffs, that the experimental images exhibit. The lack of flat-fielding information for the x-ray camera leads to intensity variations across experimental images that are not
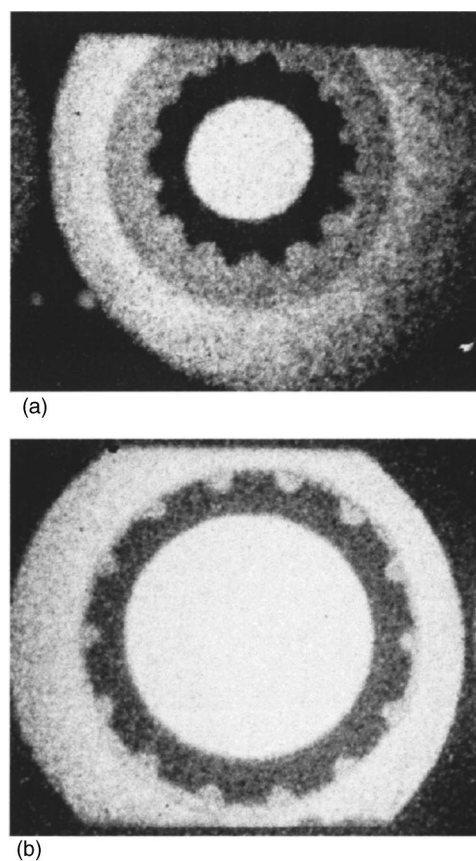

(a)

(b)

FIG. 5. (a) X-ray radiograph of small static target for shot 18 709. (b) X-ray radiograph of large static target for shot 16 520. Note the polystyrene overcoat just outside the gear shape.

recreated in simulated images. Since the simulated images do not replicate the experimental conditions exactly, the response to the filters is different. Similar to analyses of earlier data, the experimental and simulated static target images displayed different levels of sensitivity to the filtering.

Most of the experimental image detail needed to be included to achieve adequate comparisons between experiment and simulation. This detail included aspects of the image that had nothing to do with the experimental data such as the position of the imaging aperture in the radiograph. A primary image component that could not be quantified for simulation was the noise in the experimental images. The appropriate filtering levels that apply to all images could not be determined without proper characterization of this noise. After encountering these difficulties in the attempt to benchmark the Fourier filtering routines,[13] a new approach to the image analysis was sought. A key aspect of this approach would be to minimize user input in order to maintain consistency in the image analysis of any radiograph whether it is experimental or simulated.

IV. EDGE EXTRACTION ALGORITHM

The vital piece of information that must be obtained in the cylindrical implosion experiments is the shape of the embedded marker layer. The shape of this marker layer determines how much perturbation growth has occurred and serves as the primary diagnostic to compare between simu-

lation and experiment. The border between the dark band of the marker layer and the brighter surrounding areas can be defined as an edge in the image. The goal of the new image analysis process is to identify where this large intensity gradient occurs in the presence of noise. A further requirement is that the new process does not modify the edge location in the original image.

A five-step process was developed to accomplish this goal: (1) image quality improvement and noise reduction, (2) edge enhancement, (3) edge detection, (4) contour extraction by the user, and (5) contour Fourier analysis. The old procedure was similar but new image filters replace the Fourier filters formerly used in steps (1) and (2). Step (3) has been added while steps (4) and (5) remain the same.

Step (1) uses two applications of the hybrid-median filter from Nieminen.[14] Image quality and noise reduction filters attempt to reduce the background noise in an image. Some simple examples of this type of filter would be an averaging filter or a median filter. Step (2) is the application of an edge enhancement filter based on a human visual system model.[15,16] An edge enhancement filter is designed to magnify the gradient of any given edge in an image while suppressing spurious features from noise. The result of this filter does not necessarily produce an image where the edges stand out, but it can smooth noisy data near the edge while maintaining the magnitude of the intensity gradient. Step (3) accomplishes edge detection with a local algorithm from Frei and Chen.[17] Since edges are characterized by steep gradients in the pixel intensity of the image, edge detection filters are usually gradient-type operators. The resulting image will highlight the edges of objects in the image. The difficulty with these types of filters is to avoid phantom edges caused by noise in the image. Additionally, the gradient at each pixel must be a weighted sum of the gradient in the horizontal, vertical, and diagonal directions of the image.

The contour extraction process [step (4)] requires the user to define a set of points that describes the edge of interest in the image. Generally, this can be achieved by software that allows the user to ''point and click'' on the output image of the edge detection filter [see Fig. 6(b)]. Ideally, this process should be automated, but typical routines that identify contours of constant intensity are not sufficient to be used in this process because the image intensity is not uniform across the image due to the backlighter profile and lack of flat-field information for the gated x-ray camera. The final step is to decompose the user-defined contour into a modal spectrum via a fast Fourier transform (FFT). Steps (4) and (5) are accomplished using readily available scientific analysis software.

Steps (1)–(3) in the above algorithm are performed by a set of image filters chosen for their relative ease of use, lack of user input, and local neighborhood design. Local neighborhood methods are effective at edge localization and detection because image contrast boundaries are small, highly localized features. The new noise reduction and edge enhancement routines use the pixels in an $n \times n$ neighborhood around the current pixel to determine its filtered value. The old routines are considered global because a modified Fourier transform of the entire original image was used to deter-
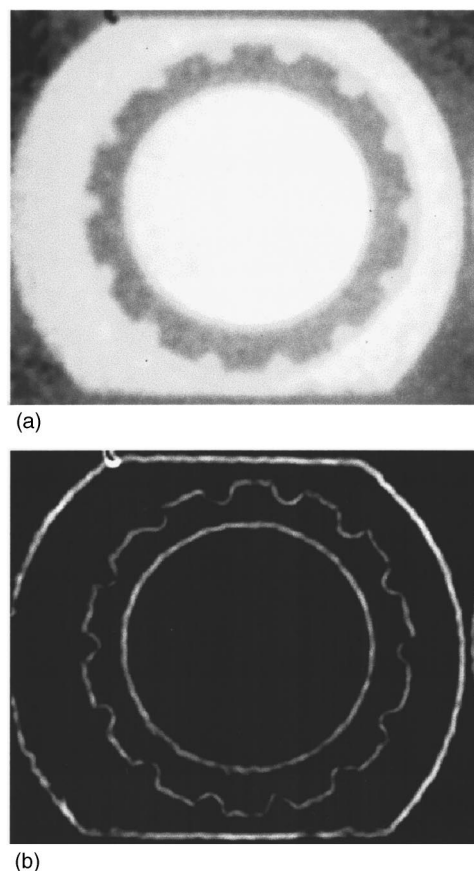

(a)

(b)

FIG. 6. (a) The result of applying noise reduction and edge enhancement to the image in Fig. 5(b). (b) Application of edge detection to the image in (a).

mine the value of each pixel in the filtered image. The older routines required the user to specify the filtering parameters (the spatial frequencies for the low-pass and high-pass filter) for each image. The lack of user input in the new routines assures that all images are filtered identically. Figure 6 demonstrates the results of steps (2) and (3) on the experimental image from Fig. 5(b).

User selection of contours adds subjective ambiguity to inferred perturbation amplitudes. If the user incorrectly defines points along the edge, the perturbation amplitudes will be inaccurate. The addition of edge detection, step (3), to the new image analysis process was meant to reduce bias introduced by the user selection of contours in step (4). The previous algorithm required the user to extract a contour from the image after the application of the Fourier filters. This required the filtered image to be displayed using a color scale. The user would select the contour by choosing points around the perturbed edge of the same color. User bias was introduced depending on which color each individual user chose as the color representing the perturbed edge. Edge detection identifies the position of the edge in the noise-reduced and edge-enhanced image helping to reduce bias introduced by user selection of contours.

V. IMAGE DEGRADATION

The new image analysis algorithm described in the previous section was applied to images of six static targets.
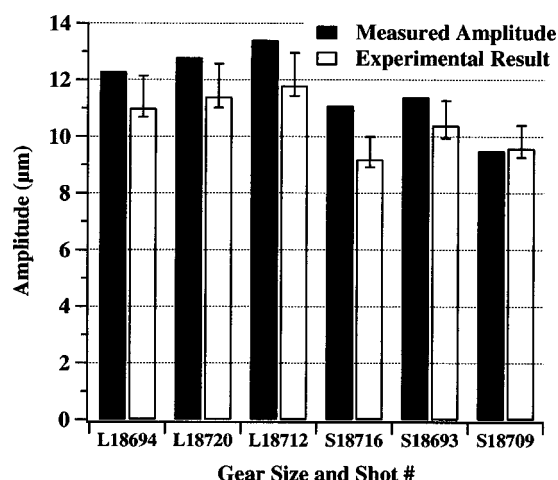
FIG. 7. Measured mode 14 amplitudes from profilometry before radiographic experiment compared to analysis of experimental images by new image processing routines. The shot number on the bottom axis is preceded by a letter denoting the gear size (*L* for large and *S* for small).

FIG. 8. Two small static target images from shot 18 709. Image (a) nominally has $\sim 1°$ of parallax and image (b) nominally has $\sim 3°$ of parallax. The inner low-density foam in both images has an oval shape due to the parallax. The effect is more pronounced in image (b). The gear teeth nearly disappear at the 10 and 4 o'clock positions.

Figure 7 shows the result of this analysis and compares it to the actual mode 14 amplitude as measured before the experiment. Five of the six experimental results underpredict the measurements from the initial condition by 1.0–1.5 μm indicating that there is a systematic process reducing or degrading the amplitude in these x-ray images. Reasons include finite image resolution and the modulation transfer function (MTF) of the imaging system, smoothing by image processing routines, variability in the selection of user contours, parallax and noise.

Image resolution limits the size of the smallest details that can be obtained from the image. The sampling rate of the film digitizer results in a digitized image with 1.67 μm per pixel. 8 μm pinholes are used to image the targets. The MTF of the pinhole combined with MTFs of the other components in the imaging system[9,18] determine the resolution of the radiograph. Since the digitized image resolution is finer than the resolution allowed by the MTF of the x-ray imaging system, the digitized image reflects the blurred effect caused by the MTF. Objects that approach sizes between the radiograph resolution and the digitized image resolution will be blurred and have few pixels describing them allowing for a greater uncertainty to their dimensions. If an object is large enough, the large number of points required to describe the object allows for a more accurate assessment of its dimensions.

The new image processing routines do not perfectly reduce noise. Generally, the reduction of noise in an image smoothes sharp features or loses fine detail. The Gaussian backlighter intensity profile hinders the image analysis process because it reduces the absolute contrast in the image. More contrast in the image would allow for easier identification of edges. A sparsely defined contour by the user introduces uncertainty as to the exact shape of the contour. If the user does not use a sufficient number of closely spaced points he/she may inadvertently smooth out a portion of the edge.
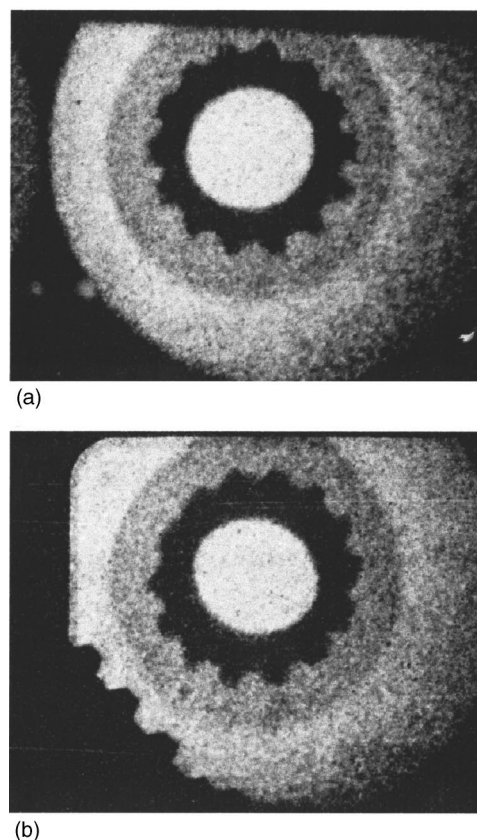
Parallax in the image distorts material interfaces. Parallax occurs when the cylindrical target is viewed off axis. Consequently, circular shapes like the inner layer of low-density foam appear oval with distorted edges. The distortion is the result of the nonaxial perspective through cylindrically symmetric features. Sixteen images are obtained for each experimental shot using a 4×4 array of pinholes. Nominally, the center of the pinhole array is aligned along the axis of the target. Therefore, all 16 images will have some degree of parallax with the worst being the corners of the 4×4 array. Figure 8 shows two separate images from the same shot. The bright region in the center of the images should be a circle. In Fig. 8(a) this appears to be true. Yet, in Fig. 8(b), the object was imaged off axis and the circle appears as an ellipse. Looking at the images in Fig. 8, one can see how the gear shape changes due to the fact it is being viewed from different angles. The effect is notably strong in Fig. 8(b) where the gear teeth nearly disappear at the 10 and 4 o'clock portions of the gear. An analysis of these images shows that the mode 14 amplitude of the gear shape in Fig. 8(b) is 2 μm less than that of Fig. 8(a). Historically, the effect of parallax has been considered small, but these experiments demonstrate how parallax causes the measured amplitude to be smaller than the actual value.

Last, image noise can affect the shape of the edge and lead the image processing routines to identify an edge falsely or to dislocate an edge. Unlike the analysis of optical depth

TABLE I. This table illustrates how image degradation mechanisms are grouped together when determining uncertainties. The effects are ranked by their relative importance for the static target experiments and whether or not their effect is to increase or decrease the amplitude of a perturbation.

	Rank	Increase amplitude	Decrease amplitude
Parallax, resolution and MTF	1	no	yes
User-defined contours	2	yes	yes
Image processing and noise	3	yes	yes

data, methods to remove noise like the Wiener filter[18] are not used in this interface-finding algorithm. Methods like Wiener filters generally require knowledge as to the type and magnitude of the noise in the image in order to remove it properly. The primary sources of noise in our experimental images are in the microchannel plate and phosphor screens of the framing camera, Poisson (photon statistical) noise from the x-ray backlighter, film grain noise, and noise from digitization of the image. The combined effect of all these sources of noise makes it difficult to characterize the noise as additive, multiplicative, or Poisson. Additionally, the parameters of the noise vary on a shot-to-shot basis making it difficult to apply these types of filters to cylindrical implosion data. These sources of noise are important to characterize for planar Rayleigh–Taylor experiments where the fluctuations in optical depth of a perturbed sample are measured.[18] Fortunately, in optical depth experiments where the modulations are one dimensional across the image, the direction parallel to the modulations can be used to characterize the noise in the image. For the cylindrical geometry experiments, where the important measurement is the physical location of the edge, precise characterization of the noise is less significant provided noise does not overwhelm the desired signal. This is not to say that noise has no effect on these results. Noise does cause dislocation of the edges in these images, but it is more important that sufficient opacity contrast is created between the transparent and opaque materials.

VI. UNCERTAINTY ASSESSMENT

Ultimately, the result of these degradation mechanisms is to place an uncertainty on the experimental result. Though one would like to treat the effect of each degradation mechanism independently of the others, this is not possible. The effect of parallax, finite image resolution and the MTF are not easily separated because one may enhance the effect of another. Noise affects how the image processing routines identify an edge. For uncertainty analysis, these image degradation mechanisms have been grouped together as shown in Table I. Table I also identifies which groups of mechanisms increase or decrease the amplitude and their relative importance.

The combined effect of parallax, resolution, and MTF was explored through a large suite of simulations of perturbed cylindrical objects. In each simulation, the amount of degradation was measured when parameters such as the perturbation amplitude, average perturbation radius, or the

amount of parallax varied. The simulations focused on a mode 14 perturbation since that was the mode of interest for these experiments. Generally, the amplitude degradation increases with increasing parallax and decreasing radius. The combined effect of this group is to reduce the amplitude and therefore only modifies the upper error bar on the data. To assess the uncertainty, a lookup table has been generated from the simulation data that gives the amount of degradation as a function of the perturbation amplitude, average radius of the perturbation, and the amount of parallax. For this experiment, the perturbation amplitude uncertainty related to this group of effects is 1.0 μm for the large static targets and 0.75 μm for the small targets. These assessments are based on one degree of parallax and the perturbation information as measured before the experiment.

Image processing combined with noise dislocates edges and modifies perturbation amplitudes. The noise reduction, edge-enhancement and edge-detection routines were tested with simulated noisy edges to gauge their ability to locate the edge under less than optimum conditions. The results of the tests quantify how much edge dislocation to expect given a signal-to-noise ratio for the edge and the number of pixels that the edge spans in the image. To evaluate the uncertainties for each experimental image analyzed by the new filtering algorithm, the user determines the ratio of the intensity change across the edge and the amount of noise. Additionally, the user must determine the distance required for the intensity change across the edge. Using this information in combination with an algorithm designed to calculate the effect of dislocating each point in the user-selected contour produces the uncertainty related to the effect of noise on the image processing routines. Examination of the static target images shows that noise in the image can dislocate the edge by one pixel on average. This translates to an average uncertainty of ~ 0.25 μm in the mode 14 perturbation amplitude for the static targets.

The uncertainty associated with a user-defined contour is determined by calculating a statistical distribution that describes the spacing between each point and its nearest neighbor in the user-defined contour. The position of the points in the contour are varied randomly according to this distribution to assess how the user's choice for the number of points in the contour modifies the perturbation amplitudes. The variation in the perturbation amplitudes is the uncertainty related to the point spacing of the contour. A novice who uses a small number of points to define a contour will have greater uncertainty than an experienced user who uses a large number of points. This routine does not assess the accuracy with which the user defines his points. Contour extraction by the user relies on the user to provide accurate positions for the location of the contour. Since the same image analysis process is applied to experimental and simulated images, this uncertainty applies to both types of images. For the simulated and experimental images, this effect resulted in ~ 0.3 μm of uncertainty when analyzed by an experienced user.

Once the uncertainty from each of the phenomena in Table I is quantified, they are added in quadrature to determine the uncertainty due to the analysis. Investigating and quantifying the sources of uncertainty have shown that the

combined effect of parallax, resolution, and the MTF is the most significant in degrading the amplitudes for this set of experiments. The other two sources of uncertainty are about 25% of the magnitude of the error introduced by the group of effects which includes parallax. This underscores that the effect of parallax must be examined in the dynamic target experiments.

VII. SIMULATION COMPARED TO EXPERIMENTAL RESULTS

The pivotal step of the benchmarking process is to compare the analysis of the experimental radiographs with simulated radiographs. Simulated radiographs of the static targets using the measured perturbation amplitudes from profilometry are generated with the LASNEX[11] and RAGE[12] codes just as performed for dynamic targets. Radiographs are generated from LASNEX data with postprocessing software that computes the absorption of backlighter photons through the LASNEX geometry along a specified line of sight over a finite time window. A time-dependent energy spectrum is specified for the backlighter source and temperature dependent material opacities are used. The RAGE code does not utilize postprocessing software and generates radiographs using a simple algorithm. The user specifies the optical depth for each material in the problem. The x-ray transmission is calculated perpendicular to the two-dimensional grid using the specified optical depths.

The size and spatial resolution of the simulated images match those of the experiment. An experimentally measured Gaussian backlighter intensity is applied to each simulated image. For these experiments, the location of the backlighter peak relative to the target axis is not measured. For this reason, the backlighter is aligned with the center of the target in the simulated images. The intensity scale of the simulated image matches that of the appropriate experimental image in order to achieve the same filter response from the image processing routines. Ideally, the effects of noise and parallax should be included in the simulated images. Currently, a model does not exist for the noise in these images. Parallax is not included in the simulated images because the current simulation method models and postprocesses only one wavelength of the perturbation. For future simulations, parallax in each experimental image will need to be assessed in order to account for its effect.

Although the RAGE calculations use a very simple model to generate the radiograph, this is sufficient for the conditions of this experiment. The opacity of the material in the static target remains constant because the target does not experience any dynamic changes. A cold opacity corresponding to the ~ 4.7 keV, helium-like line of Ti is a sufficient choice. Motion blurring is of no concern for the static target experiment. Therefore, the inability to specify a finite time window for the RAGE calculations is not important.

Simulation results are compared to the experimental results in Fig. 9. We expect the simulations to overpredict the amplitudes because of the lack of noise and parallax in the simulated images, but the predictions should fall within the experimental uncertainty. On average, the LASNEX simula-
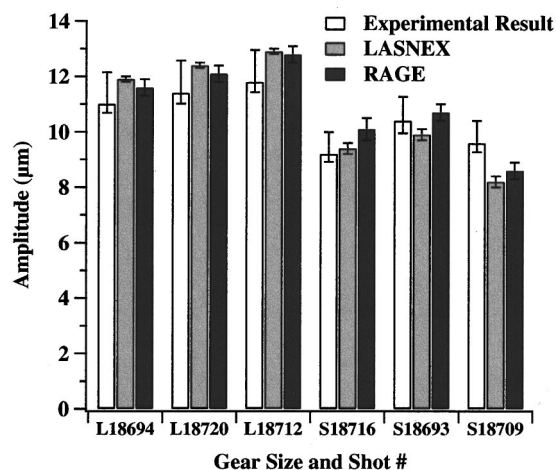

FIG. 9. Comparison of new image analysis algorithm applied to simulations and experiment. For five of the six experiments the simulations from LASNEX and RAGE are within the uncertainty of the experimental results.

tions overestimate the large static experimental results by 1 μm while RAGE overestimates by 0.7 μm. For five of the six shots the simulation results lie within the uncertainty range of the experimental data as described in the previous section. We are currently assessing the reason why the sixth piece of data from Fig. 9 does not match the predictions. For this data point both simulations underpredict the observed amplitude by ~ 1 μm or $\sim 10\%$. Given the good match with the rest of the data, this is not a significant concern but it does highlight the difficulty associated with analysis of relatively small objects in these radiographs.

VIII. SUMMARY AND CONCLUSIONS

Image processing routines used in the analysis of cylindrical implosion radiographs are benchmarked from a set of static target experiments that imaged an object of known geometry. These image processing routines are used both in the analysis of computationally simulated radiographs and experimental radiographs. Difficulty determining appropriate values of user-specified filter parameters for an older set of image reduction techniques using global, Fourier-space filters led to the development of a new algorithm using local, spatial domain operators for analyzing the radiographs. The new algorithm does not require user-specified parameters and includes a new step that detects image edges. Edge detection helps to reduce user bias in the selection of contours from the image. Mechanisms for image degradation of the experimental radiographs are identified. The effect of the image degradation is quantified as an uncertainty on the perturbation amplitudes with parallax identified as the major cause of degradation in the experimental images. Simulated radiographs generated from profilometry data of the static targets are compared to the experimental results. Analysis of the simulated images by the new image processing algorithm produces results within the uncertainties of the experimental data for five of the six experiments. These results validate the new algorithm for application to experimental data and simulations from dynamic cylindrical implosion experiments.

ACKNOWLEDGMENTS

[1] D. B. Henderson, R. L. McCrory, and R. L. Morse, Phys. Rev. Lett. **33**, 205 (1974).

[2] S. E. Bodner, Phys. Rev. Lett. **33**, 761 (1974).

[3] J. D. Lindl and W. C. Mead, Phys. Rev. Lett. **34**, 1273 (1975).

[4] J. D. Lindl, Phys. Plasmas **2**, 3933 (1995).

[5] G. I. Bell, Report No. LA-1321, Los Alamos National Laboratory, 1951.

[6] M. S. Plesset, J. Appl. Phys. **25**, 96 (1954).

[7] W. W. Hsing *et al.*, Phys. Plasmas **4**, 1832 (1997).

[8] W. W. Hsing and N. M. Hoffman, Phys. Rev. Lett. **78**, 3876 (1997).

[9] C. W. Barnes, Rev. Sci. Instrum. **70**, 471 (1999).

[10] D. L. Tubbs *et al.*, Phys. Plasmas **6**, 2095 (1999).

[11] G. B. Zimmerman and W. L. Kruer, Comments Plasma Phys. Control. Fusion **2**, 51 (1975).

[12] R. M. Baltrusaitis, M. L. Gittings, R. P. Weaver, R. F. Benjamin, and J. M. Budzinski, Phys. Fluids **8**, 2471 (1996).

[13] J. M. Scott, J. B. Beck, D. L. Tubbs, S. H. Batha, and C. W. Barnes, Bull. Am. Phys. Soc. **44**, 39 (1999).

[14] A. Nieminen, P. Heinonen, and Y. Neuvo, IEEE Trans. Pattern Anal. Mach. Intell. **9**, 74 (1987).

[15] L. Kennedy and M. Basu, Pattern Recogn. **30**, 2001 (1997).

[16] M. Basu, Pattern Recogn. **27**, 1451 (1994).

[17] W. Frei and C.-C. Chen, IEEE Trans. Comput. **26**, 988 (1977).

[18] V. A. Smalyuk, T. R. Boehly, D. K. Bradley, J. P. Knauer, and D. D. Meyerhofer, Rev. Sci. Instrum. **70**, 647 (1999).